Experimental Mechanics (2014) 54:935–942
DOI 10.1007/s11340-013-9786-6

Detecting Solid Masses in Phantom Breast Using Mechanical Indentation

L. Sallaway · S. Magee · J. Shi · O. Lehmann · F. Quivira · K. Tgavalekos · D.H. Brooks · S. Muftu · W. Meleis · R.H. Moore · D. Kopans · K.-T. Wan

Received: 27 March 2013 / Accepted: 8 July 2013 / Published online: 12 April 2014

Abstract Palpation is an economical, safe and effective method to detect breast cancer among other expensive and sometimes limited diagnostic tools such as mammography and magnetic resonance imaging (MRI). To understand the mechanics of palpation, a rigid inclusion was embedded in a phantom gel to simulate the lesion. An array of indents using a rigid indenter was made over an assigned area of the phantom surface, while the applied load, F, was measured as a function of instantaneous indentation depth, w. When the local stress field interacted with a sufficiently shallow inclusion, the mechanical response $F(w)$ yielded an augmented apparent stiffness C. A 2-dimensional spatial map of C shows the presence, depth, and geometry of the simulated lesion. A camcorder was used to capture the *in-situ* movement of the inclusion during indentation, which showed consistency with the finite element (FEA) prediction. Results provide preliminary confirmation that mechanical indentation is a good tool to complement existing imaging techniques and has the potential to guide design and fabrication of an automatic palpation device.

Keywords Palpation · Indentation · Breast cancer · Phantom gel · Lesion detection

L. Sallaway · S. Magee · J. Shi · S. Muftu · K.-T. Wan (✉)
Mechanical and Industrial Engineering, Northeastern University, Boston, MA 02115, USA
e-mail: ktwan@coe.neu.edu

O. Lehmann · F. Quivira · K. Tgavalekos · D. Brooks · W. Meleis
Electrical and Computer Engineering, Northeastern University, Boston, MA 02115, USA

R. Moore · D. Kopans
Massachusetts General Hospital, Boston, MA 02114, USA

Introduction

Breast cancer is a leading cause of non-preventable cancer deaths among women. The death rate in the United States had previously been unchanged for at least 50 years. Since mammography had been shown to significantly reduce deaths in randomized, controlled trials [1], in the mid-1980s, there is sufficient participation to affect national statistics [2]. As expected, the following 5–7 years showed a drastic decline in mortality from breast cancer [3], and there are now more than 30 % fewer deaths per annum than would have been expected. Although therapy has improved, multiple studies have consistently shown that early detection is the main factor in reducing deaths [3–11]. Therapy saves lives when breast cancers are found earlier. Mammography screening, however, is far from perfect. It does not find all cancers and does not consistently find others early enough to result in a cure. Even were all women ages 40 and over to participate in regular mammography screening, it has been estimated that the death rate from breast cancer could be decreased by 50 % [12]. Unfortunately, there remain at present approximately 40,000 fatalities due to breast cancer. Moreover, although major efforts are underway to devise preventive measures or to develop a universal cure, none are on the horizon. Thus at the present time, the best hope of curing breast cancers remains improving our ability to detect them earlier. In particular, enhanced ability to detect mammographically occult cancers at a smaller size and earlier stage can be expected to further reduce deaths.

Breast tissues are heterogeneous, and the distribution of tissue structures in the breast differ among individuals and, indeed, for each breast. Many cancers evade mammography due to the interfering presence of the normal breast tissues. The fact that most breast cancers are stiffer and harder than the surrounding tissues has led to a number of novel electromagnetic-opto-mechanical subsurface imaging methods such as magnetic resonance imaging (MRI) [13], magnetic-resonance elastography

[14], ultrasound [15], and acoustic radiation [16], all attempting to detect tumors in early stages. Despite the many advantages, these relatively expensive and time consuming methods may miss small tumors or mistaken cysts as tumors nonetheless.

One longstanding but effective, economical and safe examination method is finger palpation during a clinical breast examination (CBE) [17, 18]. However, CBE is an art that is difficult to master and teach via apprenticeship, let alone to standardize. Automating palpation through a mechanical device is a subject of previous research. To reduce the myriad of variables present in actual biological tissues but retain scientific rigor, gelatin phantoms cast into rectangular blocks or shapes that reflect the breast geometry have been designed to mimic breast tissue, and solid inclusion inserted to simulate cancers [19, 20]. A rudimentary mechanical method reported in the literature is to apply local mechanical compression on the gel surface so that the differential mechanical responses indicate the presence of an inclusion [21, 22]. An elementary model assuming the inclusion resting on a rigid substrate was adopted for data analysis, and the force measurement was taken as direct reflection of the inclusion depth. As we will show later, this oversimplified model can lead to significant errors. It is therefore necessary to construct a rigorous and systematic solid mechanics model to extract useful information and to estimate the ultimate sensitivity and capability of the method.

In this paper, we report characterization of a phantom gel with an inclusion using mechanical indentation. Modeled on conventional palpation, the method allows one to quantify the depth, geometry, and mechanical compliance of the embedded mass. A theoretical model based on well-known contact mechanics theory will be discussed and shown to be consistent with finite element analysis (FEA). This theoretically-grounded approach provides the opportunity to develop a reliable and reproducible tool to detect tumors in the breast. Another outcome of this work is to define the feasible limits of minimum inclusion size, maximum depth, and minimum stiffness contrast with the surrounding tissue where the lesion can possibly be detected.

Theory

Comprehensive solid mechanics models for indentation in linear elastic materials, the local displacement and the associated stress–strain fields in rectilinear coordinate systems, and the constitutive relations, are readily available in the literature. However, virtually all human tissues and phantom gels under an external load are known to exercise large viscoelastic, rather than linear elastic, deformation. For the sake of simplicity and proof of concept, linear elasticity is nonetheless adopted here. The half-continuum sample surface is defined with respect to the z-axis that passes through the inclusion (Fig. 1(a)–(b)). The sample surface is defined as the x-y plane where the inclusion of radius R_0 is buried at a depth $z=-d$. To specify a point on the surface, the radial distance $r=(x^2+y^2)^{1/2}$ from the origin ($x=y=0$) is used. Another coordinate system is needed for the loading axis of the indenter of radius R. Within the gel volume, the radial distance from the indent and the angle subtended with the loading axis are given by ρ and θ. The third azimuthal angle is redundant here because of axisymmetry. For a sample without an inclusion, a point load ($R\approx 0$), F, applied at the origin ($\rho=\theta=0$) creates an indentation dimple of depth, w, along the loading axis. The local subsurface stress field is given by [23, 24]

$$\sigma_i(\rho,\theta)=\frac{F}{2\pi\rho^2}g_i(\theta) \quad \text{with } i=\rho,\theta,w \tag{1}$$

where

$$g_r(\theta) = \frac{1-2\nu}{1+\cos\theta}-3\sin^2\theta\cos\theta$$
$$g_\theta(\theta) = (1-2\nu)\left(\cos\theta-\frac{1}{1+\cos\theta}\right)$$
$$g_z(\theta) = -3\cos^3\theta$$

with ν the Poisson ratio of the gel. Without delving into the rigorous mathematics, we only state some relevant characteristics of the stress field. The mechanical stress is inversely proportional to the square of radial distance, $g_i(\rho,\theta)\propto\rho^{-2}$ such that the stress field is highly localized and diminishes rapidly away from the origin. An arbitrary border of this stress field can be chosen, for instance, when $\sigma(\rho^*)$ falls below $0.10\times\sigma_0$ with σ_0 the maximum stress within the field, the region with $\rho>\rho^*$ no longer feels the presence of the external load and is considered stress-free. Force measurement as a function of the indentation dimple depth, $F(w)$, thus yields the materials properties such as the elastic modulus of the gel, E_{gel}.

In the presence of a subsurface solid inclusion, $\sigma_i(\rho,\theta)$ will be modified accordingly [25]. If the solid mass lies outside the stress field ($\rho>\rho^*$) by virtue of being too deep or too far from the origin, both $\sigma_i(\rho,\theta)$ and $F(w)$ are left status quo and governed exclusively by the gel properties. However, if (ρ,θ) falls within the stress field ($\rho<\rho^*$), $\sigma_i(\rho,\theta)$ will be distorted accordingly and $F(w)$ will reflect the location of the inclusion. The sensitivity at which we can detect the embedded solid will be raised by several factors: (i) inclusion dimension being larger than a critical threshold such as the indenter size or the contact area at the indenter-sample interface, (ii) a large mismatch between E_{gel} and E_{solid}, (which is readily satisfied in the case at hand due to the commonly accepted assumption that the lesion is 20 times stiffer than the surrounding healthy tissue [26]), and

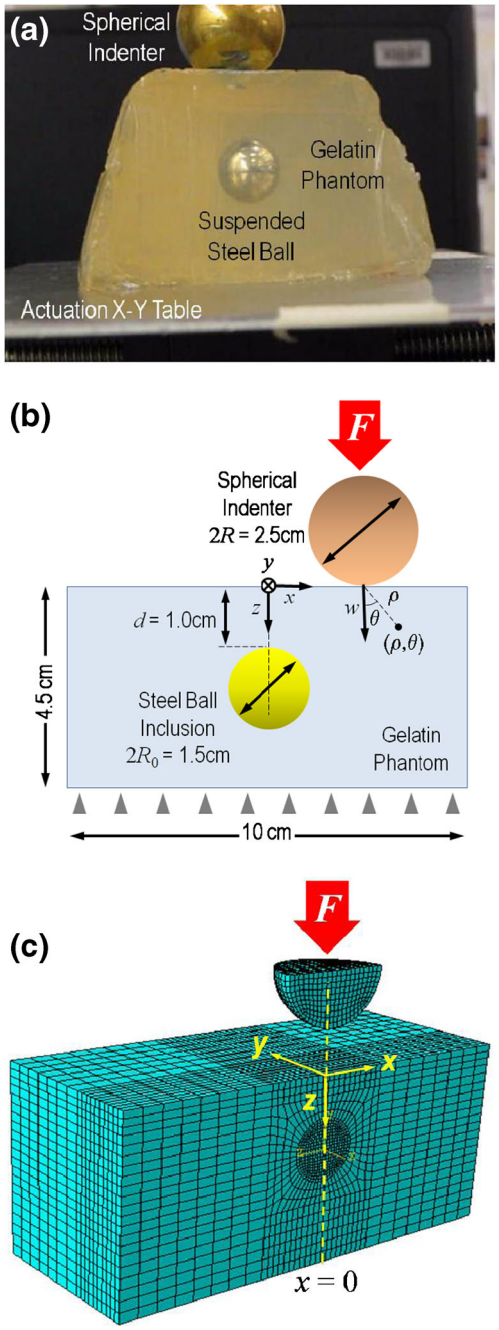

Fig. 1 Indentation of a phantom gel with solid spherical inclusion. (**a**) Portrait of a typical phantom sample. (**b**) Schematic of loading geometry. The Cartesian coordinates (x, y, z) is defined with respect to the inclusion axis ($x=y=0$) and sample surface ($z=0$). The spherical coordinates (ρ, θ) is defined with the origin at the indent ($\rho=0$, $\theta=0$). Indentation depth is w. Note that the elastic stress field in equation (1) is exact for small strain approximation and $w \to 0$. (**c**) A three dimensional mesh is set up for finite element analysis (FEA) for indentation at any location (x, y) on the surface. The indentation axis is here shown as collinear with the inclusion axis

(iii) shallow embedment under the surface with a small d. In our experiments, multiple indentations were performed perpendicular to the sample surface over a prescribed area. A two dimensional map of the apparent stiffness based on $F(w)$ is then constructed to show whether an inclusion is present.

It is worthwhile to list the model limitations upfront. The inclusion is assumed to remain fixed at its spatial location even upon interaction with the local indentation stress field. In reality, the stress gradient creates a net force that pushes the inclusion downwards and sideways (unless indentation is collinear with the inclusion axis, i.e. coincidence of z and w axes), since the soft gel is readily deformable. A rigorous mechanical model to capture the angular movement is beyond the scope of this paper. Nonetheless, as a demonstration, FEA will be employed to predict the temporal and spatial trajectory of the inclusion in response to the external load. A 3D solid model is built using a commercial FEA software ABAQUS (Standard version 6.9-2) assuming an isotropic linear elastic half-continuum gelatin phantom, a rigid half sphere indenter, and a spherical inclusion. The mechanical deformation is simulated by an 8 node reduced integration solid element (C3D8R). The gelatin was modeled by a structured mesh with ~25,000 elements, with mesh refinement at the contact area as shown in Fig. 1(c). Only half of the block was modeled due to axisymmetry. The inclusion-gel interface is taken to be strongly coupled with no slippage. The boundary conditions are set up based on: (i) symmetric boundary conditions with respect to the y-z plane, (ii) all degrees of freedoms constrained at the bottom plane of the block, (iii) a displacement constraint of indentation depth of $w=5$ mm.

Experiment

Materials

An optically transparent gelatin phantom was fabricated to match the reported average elastic modulus of normal fat tissues in the breast [26]. Mechanical integrity was ensured such that the phantom remained intact throughout the measurement without being torn apart or collapsing due to the external load. Specifically gelatin phantoms were made with a 5 to 3 ratio of Knox original unflavored gelatin packets (Kraft Foods, Tarrytown, NY) to water. The gelatin particles were dissolved in simmering water, before the solution was cooled to room temperature and then transferred to a refrigerator (4 °C). Molds were prepared by placing plastic wrap in a kidney shaped bowl to create an asymmetrical phantom to resemble the breast. Roughly 500 cc of the gel solution was then poured into the mold to 2 cm depth and cooled as described. A 1.5 cm diameter stainless steel ball was placed on the partially solidified gel and then more liquid gel solution was added to fill the container, thus suspending the solid inclusion after cooling.

A metal ball was chosen because of its high optical reflectivity for *in-situ* observation and high elastic modulus compared to the encapsulating gel. Soft microwave heating was then applied to ensure homogeneity and miscibility of the top and bottom gel layers at the interface, followed by overnight cooling.

Mechanical Characterization

Figure 1(a) and (b) show the experimental setup and a schematic. A 2.5 cm diameter metal ball was attached to a shaft that was in turn connected to the load cell of TA.XT Plus Texture Analyzer (Precision Technology, Boston, MA). The ball indented on the sample surface to an adjustable indentation depth of w=1 cm, and the mechanical response $F(w)$ measured. A 5×5 cm square area was marked on the phantom (2.5 cm on either side of the inclusion). An array of indentations was then performed by translating the phantom by a computer controlled x-y actuation table in steps of 2.5 mm along the x-axis and then repeating after a 2.5 mm shift in the y-axis. The output $F(w)$ was recorded at every lattice point of the 2-D scanned area. When the indentation was made far from the inclusion axis with large r, $F(w)$ reflected only the elastic properties of the gel, E_{gel}, that forms the baseline of mass detection. For indentation closer to the inclusion, $F(w)$ deviates from the baseline, showing the presence of solid mass underneath. By assigning a color map to the range of dF/dw, the projected geometry of the inclusion onto the sample surface, as well as the inclusion depth, was obtained. Additional experiments were performed for *in-situ* video recording of the inclusion motion upon indentation. A side camera tracked the steel ball motion as F increased from null. A tracking program ANchOVy[1] and AutoCAD were used to define the trajectory.

We note that the exact moment when the probe first touched the sample surface is crucial because any certainty will accumulate in the curve fitting routine in the logarithmic scale (see later). To determine this critical moment precisely, we started the force measurement when the probe was some small distance (~1 mm) away from the sample surface, rather than using the automatic function of the TA.XT to trigger data collection at a nonzero threshold load. The inevitable noise of the indenter disappeared suddenly at the first contact of F=0 as the viscoelastic gel dampens the random fluctuation.

[1] Video tracking software: ANchOVy, Comprehensive Software Suite for the Annotation of Objects in Videos, 2012. Authored by Oliver Lehmann, Octavia Camps, Richard Moore, and Gilead Tadmor, Northeastern University, Boston MA 02115. Contact anchovy.team@gmail.com

Results and Analysis

Figure 2 shows the force measurement $F(w)$ along a line passing directly above the inclusion. The load cell has a resolution of δF~0.1 mN and the actuator δw~10 μm. The maximum indentation depth was chosen to be w_{max}≈10 mm as indicated by the terminal data of each curve. When the indentation was performed far away from the inclusion, the probe sensed the mechanical deformation of the soft gel only and the mechanical resistance was therefore the smallest, as manifested by the gentle slope of $F(w)$ at x=2.5 cm in the right-hand curve in Fig. 2. Closer to the inclusion, the embedded sphere offers additional inertia against the indentation probe, leading to a steeper slope in $F(w)$ in the left-hand curve. Maximum stiffness was recorded when indentation was made directly above the inclusion at x=0. The complex stress–strain field in the gel around the inclusion and the resulting $F(w)$ are proved to be mathematically involved. A reasonable first approximation is to model the force measurement by a phenomenological nonlinear equation

$$F = C.w^n \tag{2}$$

where C and n are constants depending on (i) geometry: inclusion radius, indenter radius, inclusion depth, (ii) material: E_{gel}, (iii) the complex stress field due to coupled external load with the inclusion. In a log-log plot of $F(w)$ shown as an inset in Fig. 2, all curves virtually fall on the same line,

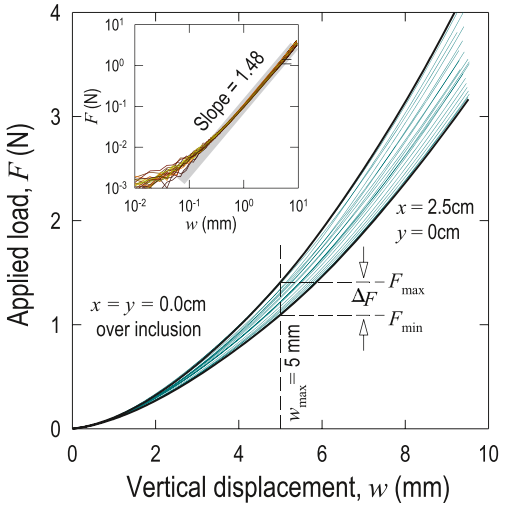

Fig. 2 Indentation over a range of (x, y) with respect to the inclusion axis was recorded by the TA.XT texture analyzer. The upper and lower bounds of the measured responses correspond to indentation at the inclusion axis (0,0) and far from the inclusion (x=2.5 cm, y=0 cm) respectively. The *inset* shows the same set of data in a logarithmic plot with an average slope of n=1.48. The large data scattering at small force and *small displacement* indicates the resolutions of the force sensing machine. Sensitivity of the indentation method is determined by the maximum indentation depth w_{max}. A force sensor is able to detect the inclusion if its resolution is better than an arbitrarily fraction of $\Delta F=F_{max}-F_{min}$

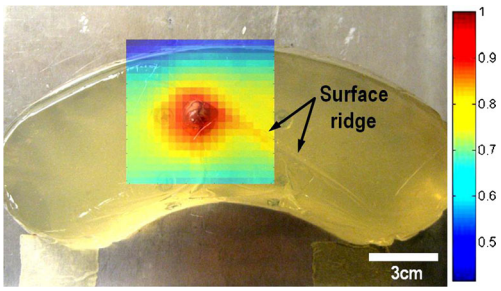

Fig. 3 Typical stiffness map overlaid on the top view of the sample surface. The *color code* indicates the normalized apparent stiffness at specific location. The *dark blue* region closely following the sample edge shows that the indenter did not touch the phantom surface. A surface ridge due to imperfect fabrication of phantom becomes apparent in the map (Color figure online)

showing equation (2) to be a reasonable representation of the mechanical response. The large data scattering at low load below 2 mN is due to the limited force resolution of the TA.XT, and is essentially ignored in our analysis. The gradient of the curve is found to be $n=d(\log F)/d(\log w)=1.48\pm0.10$, which is therefore taken as a constant for all $F(w)$ curves. Since the gel sample is isotropic, the constant C solely depends on the inclusion depth, d, and the horizontal distance from the inclusion, x. With $n=1.48$, C deduced from equation (2) is taken to be the apparent stiffness at a specific location (x,y). As alluded earlier, the first contact of the indenter with the sample surface is critical, because curve fitting in a log-log graph requires an accurate determination of the reference of $F=0$ and $w=0$. A small uncertainty can lead to significant error in determining n and C.

Figure 3 shows a two dimensional apparent stiffness map overlaid on a picture of the sample phantom. A single indentation is made at the center of each square pixel in the image, which match the lattice points described above, and the color indicates the numerical value of $C(x,y)$, normalized by its maximum value C_0 at the origin ($x=0$, $y=0$). The darkest blue region corresponds to indentation made beyond the sample edge, so that the probe did not touch the phantom surface. The apparent stiffness gradually diminishes as the indentation is made farther away from the inclusion center, as indicated. The concentric colored pattern defines the outline of the spherical inclusion. Surface texture features such as the ridge indicated in the figure are also detectable in the map. Figure 4 shows the normalized C/C_0 as a function of radial distance r for all indentation measurements. The increase in data scattering from the average values (marked as yellow circles) as r increases is the result of surface roughness and wrinkles. The lower envelop of $C(r)$ shown as gray curve is therefore a better representation of the true mechanical response of the sample. As r increases beyond 3 cm, the effect of the inclusion becomes negligible and $C(r)$

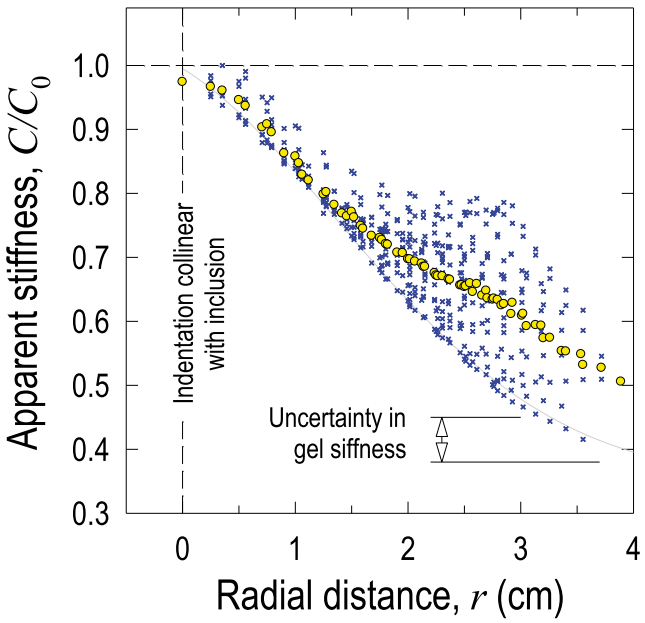

Fig. 4 Apparent stiffness, C/C_0, as a function of aerial distance, r from the inclusion axis (0,0). The mechanical stiffness is a maximum at the origin, and decreases monotonically as indentation made farther away. Large data scattering is due to surface texture. The yellow symbols denote the average value at r. The lower envelop of $C(r)$ is a good representation of the sample characteristics. An asymptotic value is found roughly 3 to 4 cm from the origin in this sample. The minimum or baseline of $C(r)$ indicates the gel elastic modulus which can be determined to certain accuracy as shown (Color figure online)

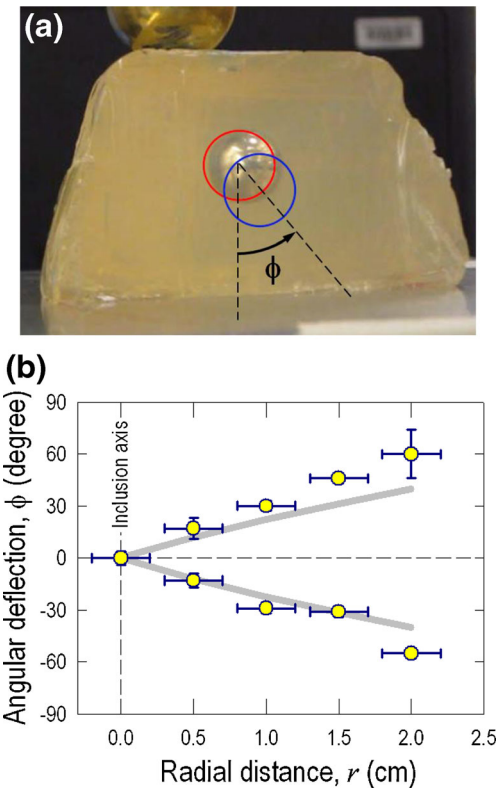

Fig. 5 Off-axis indentation where the indentation axis is not collinear with the inclusion axis. (**a**) The inclusion is pushed from the original position (*red circle*) sideways to final position (*blue*) through an angular displacement ϕ subtended to the *vertical*. (**b**) Measured ϕ (*data*) as a function of distance from the inclusion axis, along with the theoretical prediction (*curve*) derived by FEA (Color figure online)

decreases monotonically towards a fixed minimum indicating the material properties of the gel itself with no inclusion.

Figure 5(a) shows the angular displacement of the steel ball at equilibrium with the external load. The red and blue circles show the inclusion position at $F=0$ and $F=F_{max}$ respectively. A load applied directly above the inclusion with $r=0$ led to downwards movement only and there is no lateral shift with $\phi(r=0)=0^{o}$. When the load was applied off-axis a distance $r\neq 0$ from the inclusion, the stress gradient drives the ball along a curved trajectory until equilibrium is attained at an oblique angle. Figure 5(b) shows the angular displacement measured as a function of the off-axis distance $\phi(r)$, and the FEA prediction with symmetry about $\phi=0^{o}$. A reasonable fit is obtained at small r but a larger deviation is found at roughly $r>2$ cm presumably due to large deformation not explained by linear elasticity and small strain approximation.

Discussion

Our preliminary work suggests that the simple indentation method is a viable method for detecting some breast cancers. It is worthwhile to comment on a number of characteristics, limitations and improvements on the indentation technique. The size of the probe in the present study is roughly the dimension of a fingertip in order to resemble the physician's palpation. If the inclusion is arbitrarily 10 times smaller in dimension, it is unlikely that the mass will be detected. However, it is possible to use a smaller indenter probe to yield more precise information about the size and geometry of the inclusion, though more time is needed to cover the two dimensional mapping. One possible remedy is to conduct a quick and coarse scan over a large area with a smaller number of indentations before a more costly fine-scan over a suspected region. The indentation depth is also critical to determine the technique's sensitivity. If the geometrical ratio (w_{max}/d) falls below roughly 5 to 10, that is, the inclusion is too deep or the indentation depth too shallow, a perceivable change in apparent stiffness is unlikely. The numerical sensitivity can be estimated using the $F(w)$ data in Fig. 2. Discernible difference between maximum load recorded directly above the inclusion and the minimum load far from the inclusion, $\Delta F=F_{max}-F_{min}$ determines whether the inclusion can be identified by a physician's finger or an electronic sensor. For instance, in case of $w_{max}=5$ mm, $\Delta F\approx 0.3$ N and the sensor resolution should be $\delta F\approx 0.05$ N or better. The maximum depth of a discernible inclusion can also be estimated in similar manner by an equivalent reduction of w_{max} in the graph.

The present work is a proof of concept based on a primitive but readily available solid mechanics model of indentation

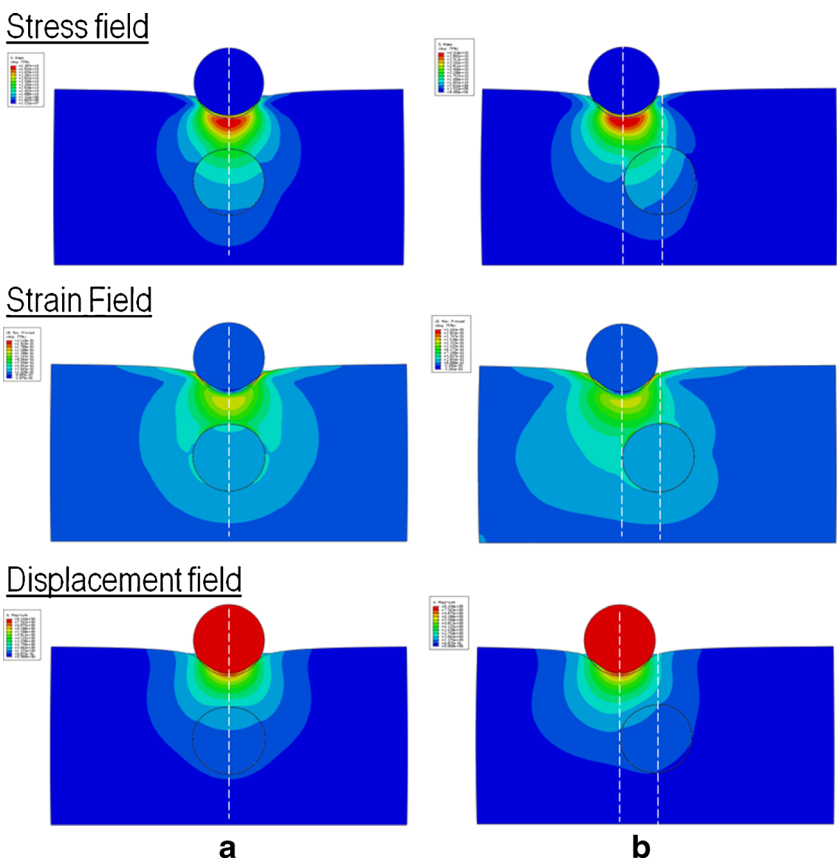

Fig. 6 (**a**) The axisymmetric von Mises stress/strain and displacement fields computed by FEA for indentation made directly above the inclusion. The mechanical stress is localized around the indent and the intermediate distance between the indent and inclusion. (**b**) The skewed fields computed for off-axis indentation

(c.f. equation (1)). Despite the inability to account for lateral motion of the inclusion upon external load (c.f. Fig. 5), FEA yields a number of interesting consequences. Figure 6(a) shows the fields of von Mises stress, strain and displacement in the sample when indenting directly above the inclusion with w_{max}=5 mm. The stress distribution remains symmetric along the loading axis, reaches its maximum immediately underneath the indenter, and fades away from the origin. Around the inclusion, the stress field is severely distorted and becomes discontinuous at the inclusion-gel interface due to the large mismatch in elastic moduli. Figure 6(b) shows the modification when the loading axis is off-center by 12.5 mm and w_{max}=5 mm. The stress field turns asymmetric and skewed towards the inclusion. It is noted that the stress and displacement are localized in the vicinity of the loading point as expected. Should the inclusion be buried at a depth much larger than w_{max}, it will not distort the stress field and thus become undetectable by this scheme.

Our ultimate goal is to expand on this preliminary work to try to develop a mechanical "palpater" in an effort to improve clinical breast examination. Such new mechanical devices can potentially detect breast lesions that are otherwise occult to mammography screening. In addition to developing a clinically viable system for testing *in vivo*, our parallel goal is to link the approach to Digital Breast Tomosynthesis (DBT) which provides high resolution, quasi three-dimensional, x-ray information on the structures of the breast. In this way we may able to monitor the internal structures of the breast as they deform during indentation as a way to identify harder tissues that could indicate cancer.

As a last remark, it is noted that indentation has been used in the engineering community to characterize sample materials with embedded particles (e.g. [27]). However, most recent literature focuses on the fabrication of composite materials with medium to high density of nano-scale particles. Since the contact area at the indenter-sample interface is usually many times that of a single particle, the mechanical response is an average measurement that varies from nano- to micro- to macroscopic scale. In this paper, we present a macro-indentation with an inclusion with size at least that of the indenter.

Conclusion

We have demonstrated how the force sensing ability of indentation is capable of detecting the location, size and shape of a rigid solid inclusion embedded in a soft gel matrix. Our measurements are consistent with both a primitive but rigorous solid mechanics model and computational finite element analysis. The technique can be used to gauge and train the sensitivity of physician's palpation, and to define the necessary precision of the force sensing devices to detect lesion.

Acknowledgments Massachusetts General Hospital is acknowledged for funding LS, SM, FQ, and KT, and the Northeastern University Gordon Scholars Program for providing a stipend for SM. Partial support for JS and KTW by the US National Science Foundation is also acknowledged. Any opinions, findings, and conclusions or recommendations expressed in this material are those of the authors and do not necessarily reflect the views of NSF.

References

1. Smith RA, Duffy SW, Gabe R, Tabár L, Yen AM, Chen TH (2004) The randomized trials of breast cancer screening: what have we learned? Radiol Clin N Am 42(5):793–806
2. White E, Lee CY, Kristal AR (1990) Evaluation of increase in breast cancer incidence in relation to mammography use. J Natl Cancer Inst 82:1546–1552
3. Kopans DB (2002) Beyond randomized, controlled trials: organized mammographic screening substantially reduces breast cancer mortality. Cancer 94:580–581
4. Tabar L, Vitak B, Tony HH, Yen MF, Duffy SW, Smith RA (2001) Beyond randomized controlled trials: organized mammographic screening substantially reduces breast carcinoma mortality. Cancer 91:1724–1731
5. Duffy SW, Tabar L, Chen H, Holmqvist M, Yen M, Abdsalah S, Epstein B, Frodis E, Ljungberg E, Hedborg-Melander C, Sundbom A, Tholin M, Wiege M, Akerlund A, Wu H, Tung T, Chiu Y, Chiu C, Huang C, Smith RA, Rosen M, Stenbeck M, Holmberg L (2002) The impact of organized mammography service screening on breast carcinoma mortality in seven Swedish counties. Cancer 95:458–469
6. Otto SJ, Fracheboud J, Looman CWN, Broeders MJM, Boer R, Hendriks JNHCL, Verbeek ALM, de Koning HJ (2003) Initiation of population-based mammography screening in Dutch municipalities and effect on breast-cancer mortality: a systematic review. Lancet 361:411–417
7. van Schoor G, Moss SM, Otten JD, Donders R, Paap E, den Heeten GJ, Holland R, Broeders MJ, Verbeek AL (2011) The National Evaluation Team for Breast Cancer Screening. Increasingly strong reduction in breast cancer mortality due to screening. Br J Cancer 104:910–914
8. Otto SJ, Fracheboud J, Verbeek AL, Boer R, Reijerink-Verheij JC, Otten JD, Broeders MJ, de Koning HJ (2012) the National Evaluation Team for Breast Cancer Screening. Mammography screening and risk of breast cancer death: a population-based case–control study. Cancer Epidemiol Biomarkers Prev 21(1):66–73
9. Swedish Organised Service Screening Evaluation Group (2006) Reduction in breast cancer mortality from organized service screening with mammography: 1. Further confirmation with extended data. Cancer Epidemiol Biomarkers Prev 15:45–51
10. Hellquist BN, Duffy SW, Abdsaleh S, Björneld L, Bordás P, Tabár L, Viták B, Zackrisson S, Nyström L, Jonsson H (2011) Effectiveness of population-based service screening with mammography for women ages 40 to 49 years: evaluation of the Swedish Mammography Screening in Young Women (SCRY) cohort. Cancer 117(4):714–722
11. Coldman A, Phillips N, Warren L, Kan L (2007) Breast cancer mortality after screening mammography in British Columbia women. Int J Cancer 120(5):1076–1080
12. Feig S (1995) Estimation of currently attainable benefit from mammographic screening of women aged 40–49 years. Cancer 75:2412–2419
13. Kopans D (2006) Breast Imaging, 3rd edn. Lippincott Williams & Wilkins, New York
14. Mariappan YK, Glaser KJ, Ehman RL (2010) Magnetic resonance elastography: a review. Clin Anat 23(5):497–511. doi:10.1002/ca.21006

15. Han L, Noble JA, Burcher M (2003) A novel ultrasound indentation system for measuring biomechanical properties of *in vivo* soft tissue. Ultrasound Med Biol 29(6):813–823
16. Radicke M, Mende J, Kofahl A, Wild J, Ulucay D, Habenstein B, Deimling M, Trautner P, Weber B, Maier K (2011) Acoustic radiation contrast in MR images for breast cancer diagnostics—initial phantom study. Ultrasound Med Biol 37(2):253–261. doi:10.1016/j.ultrasmedbio.2010.11.005
17. Mahoney L, Csima A (1982) Efficiency of palpation in clinical detection of breast cancer. Cancer Med Assoc J 127(8):729–730
18. Goodson WH III, Hunt TK, Plotnik JN, Moore DH II (2010) Optimization of clinical breast examination. Am J Med 123(4):329–334
19. Madsen EL, Frank GR, Krouskop TA, Varghese T, Kallel F, Ophir J (2003) Tissue-mimicking oil-in-gelatin dispersions for use in heterogeneous elastography phantoms. Ultrason Imaging 25:17–38
20. Lai JCY, Soh CB, Gunawan E, Low KS (2010) Homogeneous and heterogeneous breast phantoms for ultra-wideband microwave imaging applications. Prog Electromagn Res 100:397–415
21. Yegingil H, Shih WY, Shih W-H (2010) Probing model tumor interfacial properties using piezoelectric cantilevers. Rev Sci Instrum 81:095104. doi:10.1063/1.3482055
22. Yegingil H, Shih WY, Shih W-H (2007) Probing elastic modulus and depth of bottom-supported inclusions in model tissues using piezoelectric cantilevers. Rev Sci Instrum 78:115101. doi:10.1063/1.2793502
23. Johnson KL (1985) Contact Mechanics. Cambridge University Press, Cambridge
24. Maugis D (2000) Contact, Adhesion and Rupture of Elastic Solids. Springer, New York
25. Eshelby JD (1957) The determination of the elastic field of an ellipsoidal inclusion, and related problems. Proc R Soc Lond A 241:376–396
26. Krouskop TA, Wheller TM, Kallel F, Garra BS, Hall T (1998) Elastic moduli of breast and prostate tissues under compression. Ultrason Imaging 20:260–274
27. Yan W, Pun CL, Wu Z, Simon GP (2011) Some issues on nanoindentation method to measure the elastic modulus of particles in composites. Compos Part B 42:2093–2097